ADVANCED MATERIALS
www.advmat.de

An Ultrabroadband Mid-Infrared Pulsed Optical Switch Employing Solution-Processed Bismuth Oxyselenide

Xiangling Tian, Hongyu Luo, Rongfei Wei, Chunhui Zhu, Qianyi Guo, Dandan Yang, Fengqiu Wang, Jianfeng Li, and Jianrong Qiu**

Pulsed lasers operating in the mid-infrared (3–25 μm) are increasingly becoming the light source of choice for a wide range of industrial and scientific applications such as spectroscopy, biomedical research, sensing, imaging, and communication. Up to now, one of the factors limiting the mid-infrared pulsed lasers is the lack of optical switch with a capability of pulse generation, especially for those with wideband response. Here, a semiconductor material of bismuth oxyselenide (Bi_2O_2Se) with a facile processibility, constituting an ultrabroadband saturable absorber for the mid-infrared (actually from the near-infrared to mid-infrared: 0.8–5.0 μm) is exhibited. Significantly, it is found that the optical response is associated with a strong nonlinear character, showing picosecond response time and response amplitude up to ≈330.1% at 5.0 μm. Combined with facile processibility and low cost, these solution-processed Bi_2O_2Se materials may offer a scalable and printable mid-infrared optical switch to open up the long-sought parameter space which is crucial for the exploitation of compact and high-performance mid-infrared pulsed laser sources.

The mid-infrared (mid-IR) spectral region plays a crucial role in underpinning and generating future technologies because it covers the important atmospheric windows of 3–5 μm and the molecular fingerprints of numerous gases, liquids, and solids, leaving distinctive spectral fingerprints.[1–3] Moreover, 3 μm light sources have promising applications in human tissue mapping, remote sensor, radar, optical communication, as well as semiconductor microstructuring.[4,5] For this reason, both discrete and broadband mid-IR sources arouse enormous interest due to a wide range of potential applications as remote or real-time spectroscopy. To exploit the mid-IR region effectively requires the development of a raft of mid-IR fiber laser, especially the compact mid-IR pulsed fiber laser. The key component to achieve compact pulsed operation is a nonlinear optical device called a passive saturable absorber, also termed optical switch, which can generate short pulse output through switching the absorption on an ultrafast timescale.[6–8] Owing to the poor availability of the mid-IR gain materials, the development of the mid-IR short pulsed laser is mainly based on near-infrared (NIR) sources and nonlinear frequency conversion.[2,9,10] Benefiting from the rapid maturing of mid-IR gain materials, the pursuit on saturable absorbers with the performance levels on par with their NIR counterparts is intensified in recent years, especially with broadband operation wavelength.[1,5,11] Although a saturable absorber may take different physical forms, semiconductor saturable absorber mirrors (SESAMs) are widely used to generate short pulse output in fiber lasers at present; nevertheless, their operation range is narrow bandwidth and the long-wavelength access is typically limited to be ≈3 μm.[10] Researches on nanomaterials, including carbon nanotubes,[8,12,13] graphene,[7,14] nanometer-scale metamaterials,[15–19] transition metal dichalcogenides, and black phosphorus[20–23] have witnessed their great potential for the development of novel saturable absorbers. However, the intrinsic nonlinear optical response mainly in the short wavelength stimulates these materials to usually serve as the most prevalent approach for short pulse generation in NIR. Despite being a successful optical switching solution near 3 μm (due to zero bandgap),[24] graphene-based saturable absorbers have a low absorption coefficient (≈2.3%),[25,26] which hinders their application to generate short-pulse laser in mid-IR. Therefore, the introduction of a wide range of new functional materials used for the short pulse generation in the mid-IR will open new horizons and huge opportunities for a growing range of application for the mid-IR light sources.

Dr. X. Tian, Dr. Q. Guo, Dr. D. Yang, Prof. J. Qiu
State Key Laboratory of Luminescent Materials and Devices
School of Materials Science and Engineering
South China University of Technology
Wushan Road 381, Guangzhou 510641, P. R. China
E-mail: qjr@zju.edu.cn

Dr. H. Luo, Prof. J. Li
School of Optoelectronic Information
University of Electronic Science and Technology of China
Chengdu, Sichuan 610054, P. R. China
E-mail: lijianfeng@uestc.edu.cn

Dr. R. Wei
Department of Physics
Zhejiang Normal University
Jinhua, Zhejiang 321004, P. R. China

Dr. C. Zhu, Prof. F. Wang
School of Electronic Science and Engineering
Nanjing University
Nanjing 210093, China

Prof. J. Qiu
State Key Laboratory of Modern Optical Instrumentation
College of Materials Science and Engineering
Zhejiang University
Hangzhou, Zhejiang 310027, P. R. China

The ORCID identification number(s) for the author(s) of this article can be found under https://doi.org/10.1002/adma.201801021.

DOI: 10.1002/adma.201801021

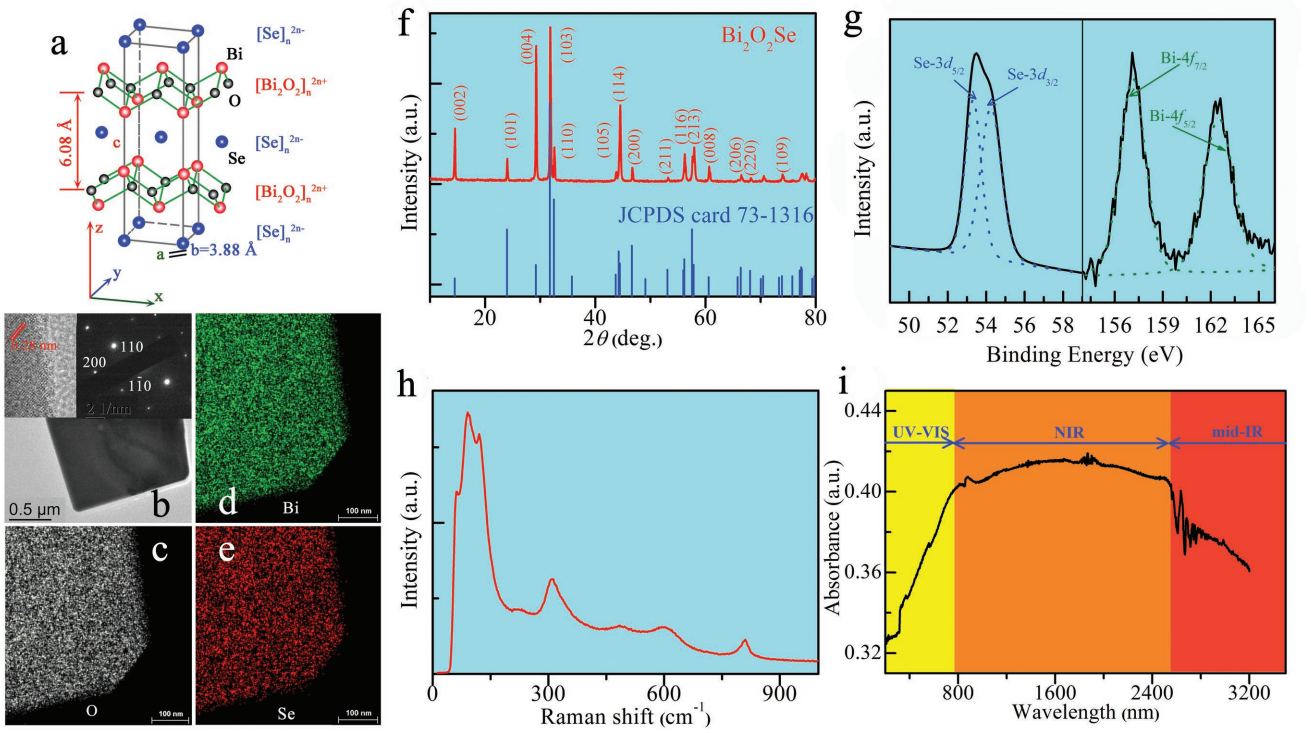

Figure 1. Lattice structure and characteristic of obtained Bi_2O_2Se. a) Crystal structure of Bi_2O_2Se, where tetragonal $[Bi_2O_2]_n^{2n+}$ layers and $[Se]_n^{2n-}$ layers are alternately stacked. Here, for clarity, the weak electrostatic interactions between the $[Bi_2O_2]_n^{2n+}$ and $[Se]_n^{2n-}$ layers are not mentioned. b) Low-magnification TEM image of a square Bi_2O_2Se. The inset contains high-resolution (HR) TEM image (left) and the SAED pattern (right). c–e) Corresponding elemental maps for O (c), Bi (d), and Se (e). f) X-ray diffraction (XRD) pattern for the as-prepared Bi_2O_2Se. g) XPS characterization of Bi_2O_2Se. h) Raman spectrum excited using a laser of 532 nm. i) Linear optical absorption. All the measurements are recorded at room temperature.

As a typical bismuth-based oxychalcogenide material, layered bismuth oxyselenide (Bi_2O_2Se) shows high electron mobility (3000 $cm^2\ V^{-1}\ s^{-1}$ at 1.9 K), environmental stability, and easy accessibility to mass production.[27,28] As shown in **Figure 1**a, the Bi_2O_2Se possesses a layered tetragonal crystal structure ($I4/mmm$, $a = 3.88$ Å, $c = 12.16$ Å, and $Z = 2$), consisting of the alternating oxide layers $[Bi_2O_2]_n^{2n+}$ (positively charged) sandwiched by $[Se]_n^{2n-}$ (negatively charged) square arrays via relatively weak electrostatic interaction (without a well-defined van der Waals interaction).[29–31] Therefore, the planar $[Se]_n^{2n-}$ layers sever as an electron conducting pathway in layer Bi_2O_2Se. In the case of Bi_2O_2Se, the bonding length of Bi—Se (≈3.272 Å) is much larger than the sum (≈3.01 Å) of the effective ionic radii of Bi^{3+} (≈1.03 Å) and Se^{2-} (≈1.98 Å) as well as the distance between Bi and Se in Bi_2Se_3 quintuple layer,[27] indicating a kind of electrostatic interaction between Bi and Se layers. Unlike other 2D semiconductors, layered Bi_2O_2Se can be cleaved along Se planar, resulting in possible rearrangement of the surface atomic structure (just like the cleavage of K^+ layer in mica), which suggests, under strong photoexcitation, the layered semiconductor has a plant of nonequilibrium distribution electrons between the $[Bi_2O_2]_n^{2n+}$ and $[Se]_n^{2n-}$, especially for the surface $[Se]_n^{2n-}$ structure. Due to the conduction electron states and the valence hole states mainly constructed by the p orbitals of Bi and Se elements, the layered Bi_2O_2Se crystals are expected to possess strong spin–orbit interaction, and can construct planar topological systems through Majorana bound states.[27,32,33] The nonequilibrium electrons as well as the potential topological state can stimulate the optical nonlinearity.[34–38] However, the potential of Bi_2O_2Se in nonlinear optics has not been explored.

In this work, we show that Bi_2O_2Se-based saturable absorber possesses ultrabroadband saturable nonlinear optical response from 0.80 to 5.0 μm. The facile grown Bi_2O_2Se can also act as an ultrafast (on the picosecond scale) optical switch with operation covering at least the 1.55–5.0 μm range. Furthermore, we experimentally demonstrated that the optical modulator based on Bi_2O_2Se could afford simple, effective, low-cost, and scalable-processed nonlinear absorbers for the Q-switched fiber laser at 3 μm.

These $[Bi_2O_2]$-contained materials are usually obtained from the solid-state reactions, which have to undergo repeated sintering process for a long time, inevitably leading to some impurities.[39] Recently, despite chemical vapor deposition technique being employed to prepare Bi_2O_2Se materials, the exacting terms such as low pressure growth, accurate flow control, and complex transfer process are not conducive to scalable production as well as cost control.[27,30,32] Considering the appropriate thermodynamics as well as the strong interlayer bonding anisotropy, Zhang et al. recently synthesized Bi_2O_2S crystal using a feasible hydrothermal reaction.[39] Hence, the analog Bi_2O_2Se crystals were prepared by an adjusted method, and more details as well as possible chemical reactions can be found in the Experimental Section. Figure 1b displays a typical transmission electron microscopy (TEM) image of Bi_2O_2Se crystals, showing

the synthesized Bi_2O_2Se with a large domain size (about 1×1 μm^2 or larger, also presented in Figure S3 in the Supporting Information). The thickness of synthesized Bi_2O_2Se crystals is about 155.5 nm. As shown in Figure S4 (Supporting Information), the calculated bandgap is about 0.14 eV. High-resolution TEM, selected area electron diffraction (SAED) pattern, and energy-dispersive X-ray spectroscopy element mapping images (Figure 1d,e) are presented to confirm the crystalline quality. Figure 1f depicts a typical X-ray diffraction (XRD) patterns. All the diffraction peaks are congruent with the body-centered tetragonal structure (JCPDS: 73-1316), and no impurity peaks are observed according to the standard pattern, which indicates that the as-prepared crystals are of single phase and high purity. X-ray photoelectron spectroscopy (XPS) spectra further verify the surface chemical states of Bi_2O_2Se. The detailed view of XPS in the Figure 1g shows that the photoelectron spectrum of Bi contains two symmetric peaks of Bi $4f_{7/2}$ and Bi $4f_{5/2}$, which are centered at ≈158.7 and ≈162.6 eV (higher than those in Bi_2Se_3),[40] respectively, attributing to the fluctuation from the chemical bonding of Bi—O_x that exists in Bi_2O_2Se.[31] As elucidated in Figure 1g, the Se 3d spectrum is at ≈53.3 eV ($3d_{5/2}$) and ≈54.2 eV ($3d_{3/2}$), respectively, which is also due to the reasonable chemical shift in Bi_2O_2Se when compared to Bi_2Se_3.[31,41] A typical Raman signal of Bi_2Se_3 crystals consist of two peaks located at ≈72 (A_{1g}^1) and ≈131 cm^{-1} (E_g^2), respectively;[42] while Bi_2O_3 stretching mode corresponds to ≈98, ≈188, ≈320, and ≈450 cm^{-1},[43] respectively. The elucidated Raman shifts at ≈88, ≈121, and ≈308 cm^{-1} in Figure 1h display reasonable Raman shift in Bi_2O_2Se. Notably, as shown in Figure 1i, the absorption spectrum covers UV–vis, NIR, and mid-IR, which is defined as ultrabroadband optical response.

We then examined the nonlinear optical (NLO) response of these synthesized Bi_2O_2Se crystals through open-aperture *Z*-scan technique and pump-probe technique.[8,10,44,45] Photoexcitation and carrier relaxation are fundamental processes that are related to optical response of materials under short pulse irradiation. The pump-probe spectroscopy can be performed to investigate the electron relaxation process after pulsed irradiation to record the nonlinear optical process. **Figure 2** shows typical *Z*-scan curves of Bi_2O_2Se under the photoexcitation wavelength of 800 and 1550 nm. Excited by the incident light, electrons from the valance band jump to fill the conduction band, simultaneously the excited electrons (on the conduction band) can return to the valance band. On increasing the incident intensity (corresponding to $Z \rightarrow 0$), the excited electrons fill up a larger number of excited states; thus, the absorption becomes saturable, leading to saturable absorption-induced transparent behavior. The nonlinear saturable absorption coefficient β is,

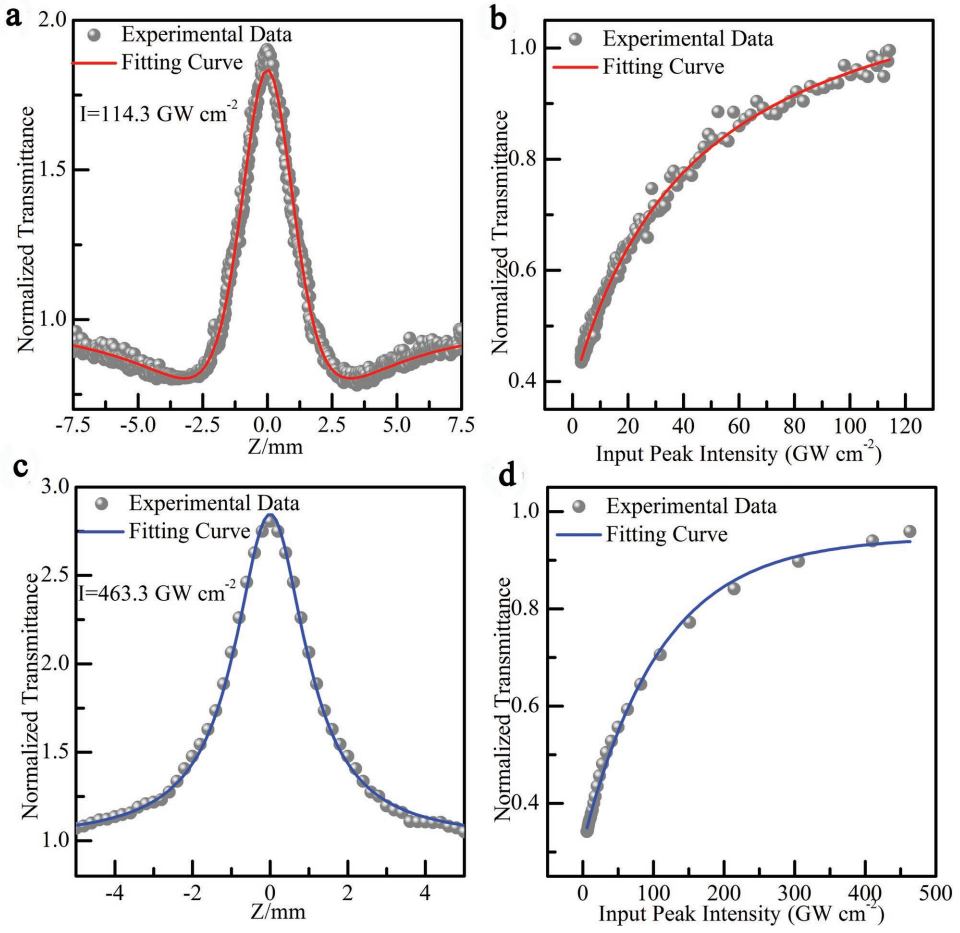

Figure 2. Experimental results and fittings measured by *Z*-scan technique. Open-aperture (OA) *Z*-scan curves under the excitation of: a) 800 nm and c) 1550 nm. The normalized transmission as a function of input power density under the excitation of: b) 800 nm and d) 1550 nm.

respectively, estimated to be about -2.91×10^{-6} cm W^{-1} (800 nm, Figure 2a) and -6.48×10^{-7} cm W^{-1} (1550 nm, Figure 2c) by fitting the *Z*-scan data according to the nonlinear absorption model (detailed discussion in the Supporting Information),[7,23] which are of orders larger than other nanomaterials such as MoS_2, $MoSe_2$, graphene, and noble metal nanocrystals (detailed comparison in Table S1 in the Supporting Information).[15,46] Furthermore, a typical closed-aperture (CA) *Z*-scan of Bi_2O_2Se was measured (presented in Figure S2 in the Supporting Information), confirming the same effect of the nonlinear phase as the effect of saturable absorption (Figure 2a,c). The dividing curves were obtained to make a distinction between the open-aperture (OA) and CA response, exhibiting a typical shape of a *Z*-scan measurement. Therefore, other nonlinear parameters such as NLO refractive index, third-order NLO susceptibility, as well as nonlinear figure of merit can be obtained to scrutinize the NLO effect based on Bi_2O_2Se. These performance parameters are comparable to previous reports realized by other nanomaterials and are summarized in Table S1 (Supporting Information). In order to evaluate the saturable absorption property under the irradiation of 800 and 1550 nm, the intensity-dependent transmittance of Bi_2O_2Se is depicted in Figure 2b (800 nm) and Figure 2c (1550 nm), respectively. The measurement data can be well fitted by a simple saturable model,[21] $T(I) = 1 - \Delta T \times \exp(-I/I_{sat}) - T_{ns}$, in which I, ΔT, I_{sat}, and T_{ns} present the input intensity, modulation depth, saturable intensity, and nonsaturable absorbance, respectively. The modulation depths are extracted to be ≈82.4% (800 nm) and ≈63.0% (1550 nm), respectively. More details can be found in the Supporting Information. These results imply strong NLO response of Bi_2O_2Se in the NIR region.

In order to investigate the NLO behavior and unravel the transient optical response of the synthesized Bi_2O_2Se in mid-IR region, a pump-probe technique was used to govern the ultrafast dynamics of excited electrons under pulse irradiation from 1.55 to 5.0 µm. It should be noted that the nondegenerated measurements provide the advantage of convenient adjustment of probe wavelength considering the ease of beam alignment (from 1.55 to 5.0 µm in this work).[10] Normalized $\Delta T/T_0$ is exhibited in **Figure 3**a to clearly display optical nonlinearity behavior from 1.55 to 5.0 µm. All the measurements in Figure 3a reveal photobleaching signatures deriving from Pauli blocking, which indicates that the synthesized Bi_2O_2Se exhibits saturable absorption over the entire spectral range investigated (1.55–5.0 µm). A blank quartz substrate is subjected to the same photoexcitation to yield no transient response, indicating that the dynamical response is related to Bi_2O_2Se. We further validate this saturable absorption response through pump fluence dependence of $\Delta T/T_0$ (1.55–5.0 µm), as depicted in Figure S3 (Supporting Information). Without any exception, all the optical responses show the typical optical-induced transparency. Figure 3b summarizes the dependence of pump power and $\Delta T/T_0$ changes. Upon a fluence of ≈26.2 µJ cm^{-2} (for a probe wavelength of 1.55 µm), a photo-induced bleaching with response amplitude of ≈13.8% records, while ≈89.8% is obtained for a probe wavelength of 5.0 µm under the same excitation fluence. On increasing the excitation fluence, the response amplitude increases as large as ≈82.6% (1.55 µm) and ≈330.1% (5.0 µm), indicating superior optical nonlinearity for long wavelength with high fluence. The large modulation depth may be attributed to the induced nonequilibrium electrons as well as potential topological state under short pulse laser irradiation.[27,32–38,47] Detailed discussion can be found in the Supporting Information. The larger response amplitude at 5.0 µm when compared to those at 1.55, 3.0, and 4.0 µm may originate from the resonance enhancement effect.[10,48–50] The transient bleaching response of Bi_2O_2Se crystals can be interpreted using the two-temperature model already developed in investigation of metallic nanocrystals and 2D crystals.[17,44,45] As shown in Figure 3a as well as Figure S6 (Supporting Information), the transient bleaching process can be fitted by a biexponential decay function, $\Delta T(t)/T = A_1\exp(-t/\tau_1) + A_2(-t/\tau_2)$,[17,45] where τ_1 and τ_2 present electron–electron coupling and electron–phonon coupling dynamics, respectively. The dynamic studies reveal that the electron–electron coupling and electron–phonon coupling dynamics happen in a short time scale

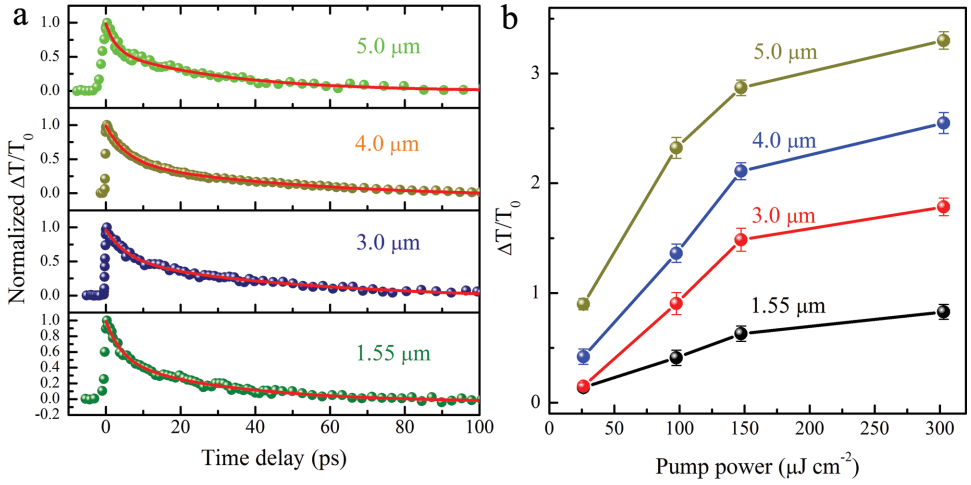

Figure 3. a) Measured transitivity transients of Bi_2O_2Se with the probe wavelength of 1.55, 3.0, 4.0, and 5.0 µm. The circles present experimental data and the red lines are the fitting curves using a two-temperature model. All the transitivity transients are normalized to their maximum transitivity. b) Pump fluence dependent measurements. The peak value of $\Delta T/T_0$ versus pump fluencies with the probe wavelength of 1.55, 3.0, 4.0, and 5.0 µm.

and a long time scale, respectively.[17] The time scale of the electron–electron coupling in a correlated electron materials is measured to be in sub-picoseconds (hundreds of femtosecond) or several picoseconds at room temperature.[8,10,17,44,45] Here, we employed a pump-probe system with a pulsed duration of 100 fs to measure the electron–electron coupling of Bi_2O_2Se crystals and the pulses' resolution can support the investigation in the shorter time scale (electron–electron coupling). The recovery time (fast component) as a function of pump fluence is presented in Figure S7 (Supporting Information). Interestingly, a fluctuation of the recovery time with pump fluence increase is observed, which may be attributed to a small increase in electron–phonon coupling time under higher pumping fluences.[51] The fast decay time (picosecond scale) is slower than heavily doped metal nanocrystals (≈393 fs for $Cu_{3-x}P$) and gold nanoparticles (≈500 fs for 15 nm gold nanoparticles),[15,17] but is consistent with that in MoS_2, $MoSe_2$, WS_2, and WSe_2 at room temperature.[44,45,48,52] Meanwhile, the recovery time at 5 µm (≈5.5 ps) is a bit faster than that in Cd_3As_2 (≈8.0 ps).[10] Owing to the difficulty of beam alignment (3–5 µm in our setup), the power-dependent transmittance under the photoexcitation of 3–5 µm has not been experimentally investigated. Even so, the saturable response and ultrafast electronic dynamics covering the mid-IR region (3–5 µm) still underpin the possible application as optical switch for mid-IR short pulse generation.

The ultrabroadband nonlinear modulation and ultrafast dynamical response in Bi_2O_2Se stimulate us to further investigate its capability for pulse generation, especially in mid-IR region. **Figure 4** shows the compact fiber laser setup at 3 µm, employing Bi_2O_2Se-based optical switch to generate the laser pulse. Two commercially available diode lasers (≈1150 nm) were used to pump the gain fiber after polarization multiplexing by a polarized beam splitter (PBS). A commercial double-cladding Ho^{3+}/Pr^{3+}-codoped ZBLAN fiber with the concentration of 30 000/2500 ppm was selected as the gain fiber. More details can be found in the Experimental Section. Increasing the launched pump power to ≈77.9 mW, stable Q-switched pulse train was first achieved, indicating that the spectra component of continuous wave (CW) is completely suppressed. The stable Q-switching regime could be maintained until the launched pump power increases up to ≈186 mW. As shown in **Figure 5**a,

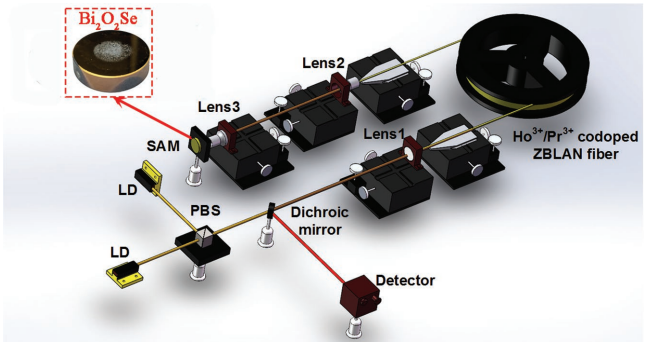

Figure 4. Schematic of the fiber laser setup for the generation of pulse laser at around 3 µm, where LD and PBS are diode laser and polarized beam splitter, respectively.

a typical Q-switching optical spectrum with a center wavelength of ≈2864.2 nm and a full-width half-maximum (FWHM) of ≈1.7 nm was obtained. Furthermore, radio frequency (RF) spectrum was also measured, exhibiting the signal-to-noise ratio of Bi_2O_2Se-based fiber laser over 42 dB at the range of typical stable Q-switching. Noteworthy, as expected for Q-switching operation, the pulse duration as well as the time interval between the adjacent pulses decreases with increasing the launched pump power. Figure 5c shows a stable Q-switched pulsed train under a pump power of ≈77.9 mW, exhibiting a time interval of ≈35.0 µs between the adjacent pulses; that is, the repetition rate is about 28.57 kHz. An individual pulse with the FWHM of ≈5.9 µs is clearly presented in the inset in Figure 5c. The repetition rate increased up to ≈62.50 kHz (corresponding to the interval time of 16 µs) when the launched pump power is increased up to ≈186 mW, meanwhile the FWHM decreased down to ≈2.0 µs. Note that the amplitude fluctuation in this process was always kept within ±2%, indicating high stability of Q-switching for practical application. If further increasing the pump power, the amplitudes of the Q-switched pulses would sharply decrease with the significantly increased repetition rate, and then rapidly turn into CW operation identified by oscilloscope. At this time, if the launched pump power was adjusted back to ≈186 mW, stable Q-switching reappeared, which indicates that the Bi_2O_2Se material was free from damage. Actually, this resulted from the oversaturation of the Bi_2O_2Se materials with the increased intracavity energy. The similar phenomenon had been observed as well in our previous Ho^{3+}/Pr^{3+}-codoped ZBLAN fiber laser Q-switched by Cd_3As_2.[10] In order to further investigate the characteristics of the Q-switched laser, the correlations between the pulse width, repetition rate, output power, as well as pulse energy and the pump power of Bi_2O_2Se-based Q-switched laser are clarified in Figure 5e,f. The repetition rate increases nearly linearly from ≈28.57 to ≈62.50 kHz, while the pulse width monotonously decreases from ≈5.9 to ≈2.0 µs, by increasing the pump power from ≈77.9 to ≈186 mW, which accords with typical Q-switched features. At the launched pump power of ≈186 mW, the maximum output power of ≈21.5 mW was obtained, giving a calculated pulse energy of ≈0.344 µJ. Although the technique is similar to other low-dimension materials (such as graphene, topological insulators, WS_2, and black phosphorus),[53–56] Bi_2O_2Se-based optical switch possesses advantages in terms of scaling to wider wavelength (0.8–5.0 µm) as well as flexibility in preparation technique.

In summary, we have demonstrated ultrabroadband optical switch covering near-infrared and mid-infrared (0.8–5.0 µm) based on a facile preparation semiconductor of Bi_2O_2Se. Obviously, saturable absorption was observed using *Z*-scan technique from 0.8 to 1.55 µm, while distinct photobleaching signatures deriving from Pauli blocking was detected from 1.55 to 5.0 µm by a pump-probe technique. Furthermore, we found the picosecond response time and response amplitude up to ≈330.1% at 5.0 µm, exhibiting large optical nonlinearity and being a potential optical switch for mid-infrared pulse laser generation. As a proof-of-concept demonstration, 2.86 µm fiber laser passively Q-switched by a Bi_2O_2Se-based saturable absorber was investigated. These demonstrations effectively reveal a step forward in the exploitation of compact mid-infrared pulsed lasers based on low-cost robust mid-IR optical

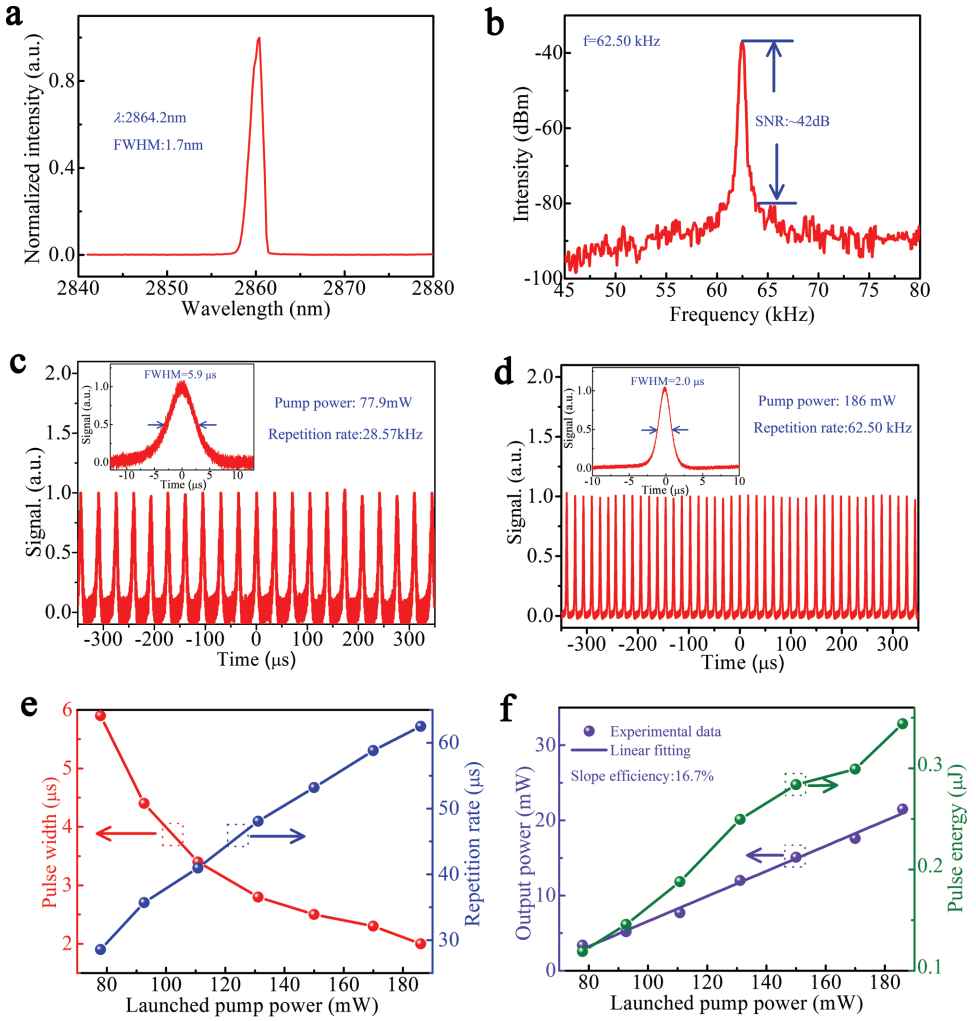

Figure 5. Q-switching characterization of Bi_2O_2Se-based mid-infrared fiber laser. a) Typical Q-switching optical spectrum. b) The RF spectrum at fundamental frequency. Typical Q-switched pulse trains at the pump power of: c) 77.9 mW and d) 186 mW. The inset is single pulse envelope. e) The pulse duration and the pulse repetition rate as a function of incident pump power. f) The output power and the pulse energy as a function of incident pump power.

switch for spectroscopy, sensing, and communication. It may be further extended to the longer wavelength (>5.0 μm) to achieve dynamic photonic and optoelectronic devices.

Experimental Section

Preparation and Characterization: 10 mL of deionized water, 4 mL hydrazine hydrate ($N_2H_4{\cdot}H_2O$, 80%), and an appropriate amount of NaOH were added in a beaker to form a hydrazine hydrate saturated alkaline solution in ultrasonic water bath. After 1 mmol Se powder (99.998%, Macklin) was added, the solution was stirred until it turned into an orange solution. 2 mmol $Bi(NO_3)_3{\cdot}5H_2O$ (99.995%, Aladdin) and 10 mL deionized water were added into a 50 mL Teflon vessel to stir thoroughly. 6.01 g $LiNO_3$ (99.9%, Aladdin) powder and 11.99 g KNO_3 (99%, Aladdin) powder were gradually added into the vessel to keep stirring for 30 min. Afterward, the orange solution was transferred into the vessel. The vessel was then sealed into stainless autoclave and the Bi_2O_2Se was synthesized under 200 °C for 24 h. The Bi_2O_2Se crystals were collected after several operations: washed 3 times by deionized water and then centrifuged at 5000 rpm for 5 min and finally dried in an oven at 80 °C for 6 h. Detailed discussion about possible chemical reactions can be found in the Supporting Information.

In order to characterize, a few droplets of the dispersion in ethyl alcohol were dropped on a quartz substrate and then dried in a vacuum oven. Raman characterization was recorded by a confocal microscopy system (Renishaw inVia, Gloucestershire, UK) excited at 532 nm at room temperature. The XRD was measured using a Bruker diffractometer utilizing Cu Kα radiation (λ = 1.5418 Å). The optical absorption spectrum was measured using a Perkin-Elmer Lambda-900 UV-Vis-NIR spectrophotometer (Perkin Elmer, Waltham, MA). An empty quartz slide was used to be as reference. X-ray photoemission spectroscopy (XPS) (K-Alpha, Thermo Science, UK) was employed to characterize the binding energies of the Se and Bi. Transmission electron microscopy (TEM) (JEOL-2100F) and field-emission scanning electron microscopy (FESEM) (Nova NanoSEM430) were used to measure the morphology. Atomic force microscopy (AFM) (Nanoscope IIIa, Veeco) was used to measure the thickness of Bi_2O_2Se crystals.

Z-Scan Measurement: The typical *Z*-scan technique was employed to measure the NLO properties under a wavelength of 800 and 1550 nm. More details can be found in Figure S1 (Supporting Information) as well as in the previous work.[23,57,58] In short, the commercial Ti:sapphire femtosecond source (1 kHz, 120 fs, and 800 nm) was equipped

with an optical parametric amplifier (OPA) to tune the wavelengths. A 0.5 mm thick quartz slide coated with Bi_2O_2Se was mounted on a linear translation stage which could move near the focus to imitate the change of the laser intensity. The laser intensity at the focus was monitored as I_0 measured by a dynamometer. The CS_2 solutions in standard quartz colorimetric utensil were set as a criterion to evaluate the *Z*-scan measurement data, with the calculated third-order nonlinear refractive index of $\approx 3.9 \times 10^{-15}$ cm^2 W^{-1} which was very close to the reported value of 3.0×10^{-15} cm^2 W^{-1}.[23] This consolidated the reliability of the experimental data.

Pump-Probe Measurement Setup: The pump-probe measurement was employed to evaluate NLO property under wide-band wavelength photoexcitation (1.55–5.0 µm). The optical source was based on an 800 nm, 1 kHz Ti:sapphire amplifier system (100 fs), as shown in Figure S2 (Supporting Information).[10] A wavelength of 800 nm with fluence of ≈300 µJ cm^{-2} was used to excite photocarriers in the Bi_2O_2Se and an OPA was used to generate probe beam with the wavelength from 1.55 to 5.0 µm. The pump light and the probe light were focused on the same point with the pump fluence 20 times stronger than that of the probe fluence. To detect the pump-induced change of probe, a PbSe detector (PDA20H, Thorlabs) with a lock-in amplifier (with a 500 Hz chopped pump) was employed in the pump-probe tests.

3 µm Fiber Laser Setup: The experimental setup of the pulsed fiber laser is shown in Figure 4. Two commercially available diode lasers (LDs) (Eagleyard Photonics, Berlin) around ≈1150 nm were used to pump the gain fiber after polarization multiplexing through a PBS and then focused by an uncoated CaF_2 plano-convex lens (LA5315, Thorlabs) (labeled as Lens1) with a 20 mm focal length. It also functioned as the collimator of the laser outcoupled from the fiber core. A dichroic mirror with a ≈96% transmittance around 1150 nm and a >95% reflectance around 3 µm was placed between the PBS and Lens1 at an angle of 45° with respect to the pump beam to direct the laser. A 3 µm bandpass filter (FB3000-500, Thorlabas) with a full-width half-maximum of 500 nm was used to block the residual pump. The used gain fiber (Fiberlabs, Japan) was a piece of commercial double-cladding Ho^{3+}/Pr^{3+}-codoped ZBLAN fiber. It had an octangular pump core with a diameter of 125 µm and numerical aperture (NA) of 0.5, and a circular core with a diameter of 10 µm and NA of 0.2. The concentration of the Ho^{3+} and Pr^{3+} were 30 000 and 2500 ppm, respectively. The selected fiber length of 7 m could provide >90% pump absorption efficiency and the pump launching efficiency was measured to be ≈82%. The fiber end close to the pump was perpendicularly cleaved as the output coupler with the help of 4% Fresnel reflection. The other end of the fiber was cleaved at an angle of 10° to avoid parasitic lasing in the cavity. First, the laser from the angle-cleaved fiber end was collimated using an uncoated ZnSe objective lens (Innovation Photonics, LFO-5-6, 0.25 NA) with a focal length of 6 mm (≈84% transmittance around 3 µm). Then, the collimated laser was focused with another same ZnSe objective lens onto the terminated feedback which was a Bi_2O_2Se/poly(vinyl alcohol) (PVA) film–coated commercial gold-protected mirror (Thorlabs), as shown in the inset of Figure 4 and also acted as the saturable absorber.

Supporting Information

Supporting Information is available from the Wiley Online Library or from the author.

Acknowledgements

X.T. and H.L. contributed equally to this work. This work was financially supported by the National Natural Science Foundation of China (Grant Nos. 51472091, 51772270, 61722503, 61435003), the National Natural Science Foundation of China (Grant Nos. 51472091, 51772270), the Guangdong Natural Science Foundation (Grant No. S2011030001349), the Fundamental Research Funds for the Central Universities (Grant No. 2013ZM0001), the Open Funds from the State Key Laboratory of High Field Laser Physics of Shanghai Institute of Optics and Fine Mechanics, Chinese Academy of Science, and the State Key Laboratory of Precision Spectroscopy of East China Normal University. This work was also supported by the Natural Science Foundation of Zhejiang Province (Grant No. LQ18A040004) and the Open Fund of the State Key Laboratory of Luminescent Materials and Devices (South China University of Technology, Grant No. 2018-skllmd-13).

Conflict of Interest

The authors declare no conflict of interest.

Keywords

Bi_2O_2Se, mid-infrared, nonlinear optical, Q-switching, saturable absorption

Received: February 12, 2018
Revised: May 2, 2018
Published online:

[1] C. R. Petersen, U. Møller, I. Kubat, B. Zhou, S. Dupont, J. Ramsay, T. Benson, S. Sujecki, N. Abdel-Moneim, Z. Tang, D. Furniss, A. Seddon, O. Bang, *Nat. Photonics* **2014**, *8*, 830.
[2] S. M. Foreman, D. J. Jones, J. Ye, *Opt. Lett.* **2003**, *28*, 370.
[3] S. D. Jackson, *Nat. Photonics* **2012**, *6*, 423.
[4] M. Fan, T. Li, S. Zhao, G. Li, H. Ma, X. Gao, C. Kränkel, G. Huber, *Opt. Lett.* **2016**, *41*, 540.
[5] A. B. Seddon, Z. Tang, D. Furniss, S. Sujecki, T. M. Benson, *Opt. Express* **2010**, *18*, 26704.
[6] U. Keller, *Nature* **2003**, *424*, 831.
[7] Q. Bao, H. Zhang, Y. Wang, Z. Ni, Y. Yan, Z. X. Shen, K. P. Loh, D. Y. Tang, *Adv. Funct. Mater.* **2009**, *19*, 3077.
[8] T. Hasan, Z. Sun, F. Wang, F. Bonaccorso, P. H. Tan, A. G. Rozhin, A. C. Ferrari, *Adv. Mater.* **2009**, *21*, 3874.
[9] C. Erny, K. Moutzouris, J. Biegert, D. Kühlke, F. Adler, A. Leitenstorfer, U. Keller, *Opt. Lett.* **2007**, *32*, 1138.
[10] C. Zhu, F. Wang, Y. Meng, X. Yuan, F. Xiu, H. Luo, Y. Wang, J. Li, X. Lv, L. He, Y. Xu, J. Liu, C. Zhang, Y. Shi, R. Zhang, S. Zhu, *Nat. Commun.* **2017**, *8*, 14111.
[11] J. Li, H. Luo, L. Wang, Y. Liu, Z. Yan, K. Zhou, L. Zhang, S. K. Turistsyn, *Sci. Rep.* **2015**, *5*, 10770.
[12] W. B. Cho, J. H. Yim, S. Y. Choi, S. Lee, A. Schmidt, G. Steinmeyer, U. Griebner, V. Petrov, D. I. Yeom, K. Kim, F. Rotermund, *Adv. Funct. Mater.* **2010**, *20*, 1937.
[13] F. Wang, A. G. Rozhin, V. Scardaci, Z. Sun, F. Hennrich, I. H. White, W. I. Milne, A. C. Ferrari, *Nat. Nanotechnol.* **2008**, *3*, 738.
[14] Z. Sun, T. Hasan, F. Torrisi, D. Popa, G. Privitera, F. Wang, F. Bonaccorso, D. M. Basko, A. C. Ferrari, *ACS Nano* **2010**, *4*, 803.
[15] S. Link, C. Burda, Z. L. Wang, M. A. El-Sayed, *J. Chem. Phys.* **1999**, *111*, 1255.
[16] X. Hu, Y. Zhang, Y. Fu, H. Yang, Q. Gong, *Adv. Mater.* **2011**, *23*, 4295.
[17] Z. Liu, H. Mu, S. Xiao, R. Wang, Z. Wang, W. Wang, Y. Wang, X. Zhu, K. Lu, H. Zhang, S.-T. Lee, Q. Bao, W. Ma, *Adv. Mater.* **2016**, *28*, 3535.
[18] M. Z. Alam, I. De Leon, R. W. Boyd, *Science* **2016**, *352*, 795.
[19] P. Guo, R. D. Schaller, J. B. Ketterson, R. P. H. Chang, *Nat. Photonics* **2016**, *10*, 267.
[20] Y. K. Srivastava, A. Chaturvedi, M. Manjappa, A. Kumar, G. Dayal, C. Kloc, R. Singh, *Adv. Opt. Mater.* **2017**, *5*, 1700762.

[21] J. Koo, Y. I. Jhon, J. Park, J. Lee, Y. M. Jhon, J. H. Lee, *Adv. Funct. Mater.* **2016**, *26*, 7454.
[22] J. Huang, N. Dong, S. Zhang, Z. Sun, W. Zhang, J. Wang, *ACS Photonics* **2017**, *4*, 3063.
[23] R. Wei, H. Zhang, X. Tian, T. Qiao, Z. Hu, Z. Chen, X. He, Y. Yu, J. Qiu, *Nanoscale* **2016**, *8*, 7704.
[24] J. Li, Y. Yang, D. D. Hudson, Y. Liu, S. D. Jackson, *Laser Phys. Lett.* **2013**, *10*, 045107.
[25] A. Martinez, Z. Sun, *Nat. Photonics* **2013**, *7*, 842.
[26] J.-U. Lee, D. Yoon, H. Kim, S. W. Lee, H. Cheong, *Phys. Rev. B* **2011**, *83*, 081419.
[27] J. Wu, H. Yuan, M. Meng, C. Chen, Y. Sun, Z. Chen, W. Dang, C. Tan, Y. Liu, J. Yin, Y. Zhou, S. Huang, H. Q. Xu, Y. Cui, H. Y. Hwang, Z. Liu, Y. Chen, B. Yan, H. Peng, *Nat. Nanotechnol.* **2017**, *12*, 530.
[28] M. Wu, X. C. Zeng, *Nano Lett.* **2017**, *17*, 6309.
[29] J. Li, Z. Wang, Y. Wen, J. Chu, L. Yin, R. Cheng, L. Lei, P. He, C. Jiang, L. Feng, J. He, *Adv. Funct. Mater.* **2018**, *28*, 1706437.
[30] J. Wu, Y. Liu, Z. Tan, C. Tan, J. Yin, T. Li, T. Tu, H. Peng, *Adv. Mater.* **2017**, *29*, 1704060.
[31] J. Wu, C. Tan, Z. Tan, Y. Liu, J. Yin, W. Dang, M. Wang, H. Peng, *Nano Lett.* **2017**, *17*, 3021.
[32] M. Meng, S. Huang, C. Tan, J. Wu, Y. Jing, H. Peng, H. Q. Xu, *Nanoscale* **2018**, *10*, 2704.
[33] R. M. Lutchyn, J. D. Sau, S. Das Sarma, *Phys. Rev. Lett.* **2010**, *105*, 077001.
[34] X. Yin, Z. Ye, D. A. Chenet, Y. Ye, K. O'Brien, J. C. Hone, X. Zhang, *Science* **2014**, *344*, 488.
[35] E. Hendry, P. J. Hale, J. Moger, A. K. Savchenko, S. A. Mikhailov, *Phys. Rev. Lett.* **2010**, *105*, 097401.
[36] Y. Li, Y. Rao, K. F. Mak, Y. You, S. Wang, C. R. Dean, T. F. Heinz, *Nano Lett.* **2013**, *13*, 3329.
[37] D. Hsieh, J. W. McIver, D. H. Torchinsky, D. R. Gardner, Y. S. Lee, N. Gedik, *Phys. Rev. Lett.* **2011**, *106*, 057401.
[38] A. V. Krasavin, P. Ginzburg, A. V. Zayats, *Laser Photonics Rev.* **2018**, *12*, 1700082.
[39] X. Zhang, Y. Liu, G. Zhang, Y. Wang, H. Zhang, F. Huang, *ACS Appl. Mater. Interfaces* **2015**, *7*, 4442.
[40] D. Kong, J. J. Cha, K. Lai, H. Peng, J. G. Analytis, S. Meister, Y. Chen, H.-J. Zhang, I. R. Fisher, Z.-X. Shen, Y. Cui, *ACS Nano* **2011**, *5*, 4698.
[41] X. Tian, R. Wei, S. Liu, Y. Zhang, J. Qiu, *Nanoscale* **2018**, *10*, 752.
[42] J. Zhang, Z. Peng, A. Soni, Y. Zhao, Y. Xiong, B. Peng, J. Wang, M. S. Dresselhaus, Q. Xiong, *Nano Lett.* **2011**, *11*, 2407.
[43] G. Sarala Devi, S. V. Manorama, V. J. Rao, *Sens. Actuators, B* **1999**, *56*, 98.
[44] G. Wang, L. Bouet, D. Lagarde, M. Vidal, A. Balocchi, T. Amand, X. Marie, B. Urbaszek, *Phys. Rev. B* **2014**, *90*, 075413.
[45] Q. Wang, S. Ge, X. Li, J. Qiu, Y. Ji, J. Feng, D. Sun, *ACS Nano* **2013**, *7*, 11087.
[46] K. Wang, Y. Feng, C. Chang, J. Zhan, C. Wang, Q. Zhao, J. N. Coleman, L. Zhang, W. J. Blau, J. Wang, *Nanoscale* **2014**, *6*, 10530.
[47] M. Kauranen, A. V. Zayats, *Nat. Photonics* **2012**, *6*, 737.
[48] N. Kumar, Q. Cui, F. Ceballos, D. He, Y. Wang, H. Zhao, *Phys. Rev. B* **2014**, *89*, 125427.
[49] J. Zhang, D. Li, R. Chen, Q. Xiong, *Nature* **2013**, *493*, 504.
[50] Q. Zhang, X. Liu, M. I. B. Utama, G. Xing, C. Sum Tze, Q. Xiong, *Adv. Mater.* **2015**, *28*, 276.
[51] B. T. Diroll, P. Guo, R. P. H. Chang, R. D. Schaller, *ACS Nano* **2016**, *10*, 10099.
[52] L. Yang, N. A. Sinitsyn, W. Chen, J. Yuan, J. Zhang, J. Lou, S. A. Crooker, *Nat. Phys.* **2015**, *11*, 830.
[53] Z. Qin, G. Xie, H. Zhang, C. Zhao, P. Yuan, S. Wen, L. Qian, *Opt. Express* **2015**, *23*, 24713.
[54] C. Wei, X. Zhu, F. Wang, Y. Xu, K. Balakrishnan, F. Song, R. A. Norwood, N. Peyghambarian, *Opt. Lett.* **2013**, *38*, 3233.
[55] J. Li, H. Luo, L. Wang, C. Zhao, H. Zhang, H. Li, Y. Liu, *Opt. Lett.* **2015**, *40*, 3659.
[56] W. Chen, L. Hongyu, Z. Han, L. Chun, X. Jitao, L. Jianfeng, L. Yong, *Laser Phys. Lett.* **2016**, *13*, 105108.
[57] R. Wei, X. Tian, Z. Hu, H. Zhang, T. Qiao, X. He, Q. Chen, Z. Chen, J. Qiu, *Opt. Express* **2016**, *24*, 25337.
[58] R. Wei, H. Zhang, Z. Hu, T. Qiao, X. He, Q. Guo, X. Tian, Z. Chen, J. Qiu, *Nanotechnology* **2016**, *27*, 305203.